Numerical investigation of thermal runaway behavior of lithium-ion batteries with different battery materials and heating conditions

Abstract：While the lithium-ion batteries (LIBs) have been developed remarkably, the proliferating fire and explosion accidents caused by thermal runaway (TR) is still the main obstacle that hinders the extensive applications of LIBs. An abuse condition triggering TR of particular interest is local heating, which is the direct and common cause of the battery TR. Despite numerous published work devoted to the numerical simulations of the LIB behaviors under thermal abuse, few studies focused on the local heating conditions and a comprehensive simulation and analysis of TR under local heating from the perspective of heat generation, external heat and heat loss still lacks. In this study, a three-dimensional TR model coupled with five exothermic decomposition reactions and internal short circuit was developed within frame of OpenFOAM to study the effects of heat generation, external heat and heat loss by simulating TR behaviors with various battery materials, external heating conditions and heat dissipation conditions. The results indicate that LIBs with $Li_4Ti_5O_{12}$ (LTO) anode shows better thermal safety and stability than the graphite anode, and LIBs with $LiFePO_4$ (LFP) cathode possesses the best thermal safety and stability compared other cathode materials. The increasing separator melting temperature was found to improve the onset temperature of TR as well as delaying the occurrence of TR. Additionally, the heating position near the bottom of LIBs was found more inclined to induce TR than other heating positions. Limiting the heating power applied to the LIB surface below 0.75 W helps the LIBs stay in the steady-state and provides effective relief from TR. The improved convection conditions and low ambient temperature were found to increase the cell tolerance against TR. These conclusions may provide references for the safe design of thermal management system of LIB packs.

Keywords: Lithium-ion battery; Thermal runaway; Local heating; Battery materials

1. Introduction

Due to environmental problems caused by the consumption of fossil fuels, such as pollution and global warming, electric energy has been widely used. The lithium-ion battery (LIB) possesses higher density of energy and the longer cycle life, and smaller environmental pollution compared with other batteries, proving high potential as the electric energy storage devices. However, fire and explosion accidents caused by thermal runaway (TR) of LIBs drew the attention of the public. TR of LIBs can be triggered by overheating, overcharge, nail penetration, crash and short circuit[1-7]. In these abuse conditions, thermal abuse is a quite common cause of LIB TR accidents, which can result in TR directly. Under elevated temperature, a series of exothermic reactions and electrochemical reactions take place leading to continued temperature rise and heat accumulation[8-11]. Once the heat generated is more than what can be dissipated, this process eventually leads to TR[11, 12]. During the evolution of TR of one single LIB and the TR propagation in LIB pack, local heating is a common way for thermal abuse causing TR. For instance, Beauregard et al.[13] reported a TR

accident of the HEV battery pack that the current-carrying joint overheated owing to looseness and heated the cell surface locally. Additionally, during the TR propagation of LIB pack, the TR of normal cell can be initiated when suffering from the heat from the adjacent cell of TR, which is a typical scenario of TR owing to local heating. Therefore, the prediction of LIB TR behaviors under local heating has remarkable significance for reducing fire and explosion accidents of LIBs.

In the recent past, some experiment studies were conducted about the thermal behavior of LIB under local heating. Weng et al.[14] studied the effects of heating modes on thermal failure propagation by a series of experiments, finding that temperature rising rate was different with different heating position, and the phenomena of TR was more violent when heating near the positive pole. Li et al.[15] investigated the TR behavior a LIB triggered by a cylindrical heater. The effects of state of charge (SOC), the power of heater and the cell spacing were studied and the amount of heat transferred between the cell and heater was calculated. Wang et al.[16] used cylindrical heater and electric furnace to heat the fully charged 50 Ah graphite/LiNi$_x$Co$_y$Mn$_{1-x-y}$O$_2$ batteries, and the effects of different heating methods, heating position, area and power were studied. They pointed out there was a higher thermal abuse hazard for battery with the increase of heating power and heating area. In spite of numerous experiments to study the influence of some key parameters on the TR behavior under thermal abuse, the experimental results are difficult to visualize the cell-internal propagation of TR. In addition, numerous experiments are required to predict the thermal behavior under more thermal abuse conditions, which are time-consuming and expensive.

Some numerical simulation studies are also conducted to reduce the time and economic burden of TR experiments and visualize the TR propagation in single cell of LIBs. Hatchard et al.[17] first proposed the lumped thermal model used for oven tests. Kim et al.[18] extended this one-dimensional model to three-dimensional model used for oven tests of cylindrical graphite/LiCoO$_2$ batteries. They found smaller cells

rejected heat faster than larger cells, contributing to prevent TR. In addition, the propagation of the abuse reactions inside the cell triggered by localized heating was also investigated in their study. Guo et al.[19] then extended the thermal model coupled with the reversible, irreversible and side reaction heat to study the temperature distribution and evolution used for the square graphite/LiFePO$_4$ cells under oven tests. The temperature gradient along thickness was found to be higher than that along width and length direction in their study. Peng et al.[20] employed a thermal model to study the temperature evolution of cylindrical graphite/LiCoO$_2$ batteries for oven tests, to investigate the influence of heat release condition and oven temperature on TR behaviors of LIBs, finding out that the critical heat release coefficient and the critical oven temperature leading to TR are negatively correlated. Lopez et al.[21] studied the thermal behavior of single graphite/LiCoO$_2$ cell during the conventional oven tests and the constant power modified oven tests. Their focus was the influence of the convection condition, cell physical configuration and electrolyte combustion. The temperature distribution variation of the separator and thermal characteristics of square NCM cell under local heating on cathode current collector were numerically studied by Zhao et al.[22]. They reported that it could prevent TR when the heat dissipation coefficient of the battery reached 10 W m^{-2} K^{-1}. Peng et al.[23] established a three-dimensional thermal model describing oven test processes and compared the thermal safety and stability of the cells with five cathode materials including LiCoO$_2$, LiNi$_{0.8}$Co$_{0.15}$Al$_{0.05}$O$_2$, Li$_{1.1}$(Ni$_{1/3}$Co$_{1/3}$Mn$_{1/3}$)$_{0.9}$O$_2$, LiMn$_2$O$_4$, and LiFePO$_4$. The LiMn$_2$O$_4$ cell was found to possess the best thermal stability and the LiFePO$_4$ was the safest cathode material.

The above-mentioned numerical studies mostly focused on oven tests that represented the condition exposed to high ambient temperature, few studies followed with interest the TR behaviors under local heating while it also has engineering application significance as mentioned above. In addition, the TR behaviors of LIBs under local heating depend on three aspects: heat generation within the cell, heat from external source

and heat loss to the ambient. The enormous heat generation is the typical characteristic of TR, leading to the rapid temperature increase, which is mainly determined by the reactions among various battery materials. The heat from external source induces the initial temperature rise to the onset temperature of TR while the heat loss on the cell surface suppresses this trend. Thus, to comprehensively understand the regularity and mechanism of LIB TR under local heating, not a single above aspect can be omitted. However, previous simulations researched the thermal abuse of LIBs only considering single or two aspects, little published work systematically and comprehensively addressed the thermal behaviors of LIBs from all the above perspective, especially lacking the investigation of various battery materials from the perspective of heat generation. In summary, a necessary study is conducting an all-directional simulation and analysis pointing at TR behaviors under local heating, aiming at providing comprehensive guidance for promoting the safe design of thermal management system (BMS) of battery packs on the inhibition on thermal propagation.

In this present study, a three-dimensional model coupling heat transfer and electrochemistry has been developed within the frame of open source computational fluid dynamics (CFD) code OpenFOAM to investigate the influence of heat generation, external heating and heat loss on the TR behaviors under local heating. The model validated by the NCA cell has been applied to investigate and rank the thermal safety and thermal stability of different battery materials (i.e. cathode, anode, electrolyte and separator) from the perspective of heat generation. This is followed by the study of some critical factors including different heating position, heater size and heating power, from the point of view of external heating. Finally, the effects of the ambient temperature and convection conditions on the heat loss on the cell surfaces are investigated. This paper is organized through 4 sections with Section 1 being introduction. Section 2 describes the electro-chemical model as well as the model validation. The influences of many critical impacting factors on the thermal behaviors of LIBs were numerically investigated in Section 3 and Section 4 summarizes the main

conclusions of this study.

2. Model Description

A three-dimensional model has been built in the frame of OpenFOAM to describe the process of TR of

LIBs. The schematic of the computational model is shown in **Fig. 1.** Schematic of the computational model..

The object of modeling in this paper is the cylindrical 18650 cell, with a diameter of 18 mm and height of 65

mm. Actually, a typical internal structure of LIBs consists of numerous thin layers: a copper current collector,

negative electrode, separator, positive electrode and aluminum current collector[23]. However, the

computation is quite large to resolve the small-scale structures, thus the jellyroll is perceived as a

homogeneous solid structure. It is assumed that the cell is locally heated in open air. The effect of the local

heating is modelled by the heat flux on the boundary. The convective and the radiative heat transfer are

considered to account for the effect of the environment cooling on the behavior of the cell.
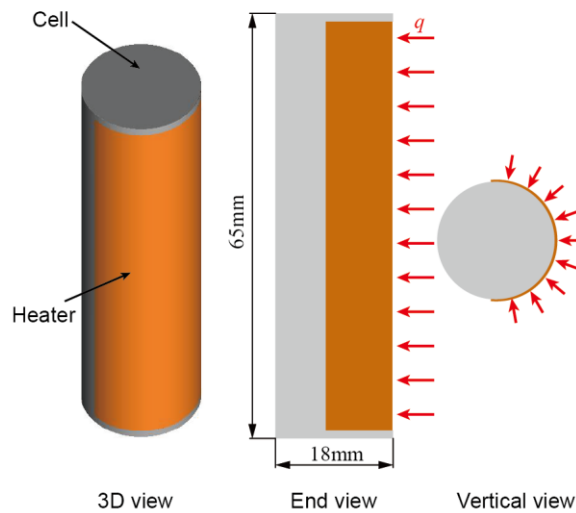
Fig. 1. Schematic of the computational model.

The flow chart of the electro-thermal model is shown in **Fig. 2**, the key steps includes: (1) creating

geometry and mesh, and determining boundary as well as initial conditions; (2) calculating the fraction of

each component based on the temperature field, and calculating the heat release rate of exothermic chemical

reactions according to the fraction, the details of the equations are given in Sections **2.2** Electrochemical

model. (3) solving energy equation to calculate temperature field, the details of the equations are given in

Sections **2.1** Thermal model; (4) substituting the temperature into first step and repeating the above steps

until end time.

```
              ┌─────────────────────────────┐
              │  Boundary & Initial conditions │
              └─────────────────────────────┘
                            │
Temperature T  ┌────────────────────────────────┐
          ─────│ Calculate the fraction of components cᵢ │
              └────────────────────────────────┘
```

$$\frac{c_i^{n+1} - c_i^n}{\Delta t} = -A_i \exp\left(-\frac{Ea_i}{RT}\right) c_i^{n+1}$$

Calculate the heat of reaction Q_i

$$Q_i = -W_i H_i \frac{dc_i}{dt}$$

Solve energy equation

$$\rho C_p \frac{\partial T}{\partial t} = \nabla \cdot (\kappa \nabla T) + \sum Q_i$$

No — Residual<=Tolerance?

Yes

Temperature field T

No — Time>=End time?

Next time step

Yes

End
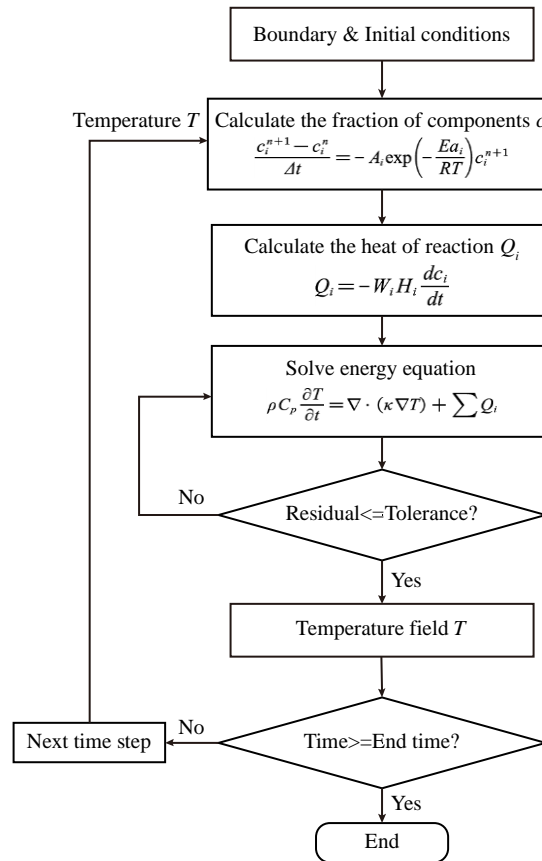
Fig. 2. Flow chart of the electro-thermal model.

2.1 Thermal model

Thermal conduction dominate internal heat transport in the cell because the convective heat transfer

through the evaporated electrolyte and production gas inside the cell can be ignored[18]. In addition to the

thermal conduction inside the cell, abuse thermal reactions between the cell materials with the elevated

temperature, including the decomposition of SEI layer, the reaction between anode and electrolyte, the

reaction between cathode and electrolyte, the decomposition of electrolyte and binder reaction[9, 10].

Therefore, the 3D heat conduction equation within the cell can be written as follows:

$$\rho C_p \frac{\partial T}{\partial t} = \nabla \cdot (\kappa \nabla T) + Q_{rec} \tag{1}$$

$$Q_{rec} = \sum Q_i = Q_{SEI} + Q_a + Q_c + Q_{ec} + Q_e + Q_{PVDF} \tag{2}$$

where ρ is the density; T is the temperature; C_p is the heat capacity, which is a function of temperature[24]; κ is the thermal conductivity; Q_{rec} is reaction heat as in Eq.(2), consisting of Q_{SEI}, Q_a, Q_c, Q_{ec}, Q_e, Q_{PVDF}. The energy equation at the boundary between the cell and the ambient is given by Eq.(3). Where h is convective heat transfer coefficient, T_{amb} is ambient temperature, ε is the surface emissivity of the cell, and σ is Stefan-Boltzmann constant. And the boundary condition between the cell and the heater is shown as Eq.(4), where q is the heat flux from the heater to cell.

$$-\kappa \frac{\partial T}{\partial n} = h(T_{amb} - T) + \varepsilon \sigma (T_{amb}^4 - T^4) \tag{3}$$

$$-\kappa \frac{\partial T}{\partial n} = q \tag{4}$$

2.2 Electrochemical model

2.2.1 Decomposition of SEI layer

Due to irreversible electrochemical decomposition of the electrolyte in solid electrolyte interphase layer, solid electrolyte interface (SEI) is formed on the graphite anode, which can protect anode from direct reaction with electrolyte[10]. When the temperature rises to a certain temperature, the SEI layer will decompose, which can be described by Arrhenius equations[17], showing as Eq.(5):

$$\frac{dc_{SEI}}{dt} = -A_{SEI}c_{SEI}\exp\left(-\frac{Ea_{SEI}}{RT}\right) \tag{5}$$

The heat release per unit volume can be characterized as follows:

$$Q_{SEI} = -W_{SEI}H_{SEI}\frac{dc_{SEI}}{dt} \tag{6}$$

where c_{SEI} is the dimensionless amount of lithium containing meta-stable species in the SEI layer; A_{SEI}

is the frequency factor; Ea_{SEI} is the activation energy; R is molar gas constant, and its value is 8.314J mol^{-1} K^{-1}; W_{SEI} is specific SEI content in jelly roll; H_{SEI} is SEI-decomposition heat release per unit mass.

2.2.2 Reaction between anode and electrolyte

Currently, graphite and Li$_4$Ti$_5$O$_{12}$ (LTO) is one of the widely used material for the anode LIBs. Exothermic reactions between anode and electrolyte will occur when the temperature rises to the onset temperature of the anode decomposition[10]. The reaction rate of anode reaction is shown as Eq.(7)[17, 25]

$$\frac{dc_a}{dt} = -A_a c_a \exp\left(-\frac{Ea_a}{RT}\right)\exp\left(-\frac{c_{SEI}}{c_{SEI,ref}}\right) \tag{7}$$

The heat release per unit volume is estimated as follows:

$$Q_a = -W_a H_a \frac{dc_a}{dt} \tag{8}$$

where c_a is dimensionless amount of lithium intercalated within the carbon; A_a is the frequency factor; Ea_a is the activation energy; $\exp\left(-\frac{c_{\text{SEI}}}{c_{\text{SEI,ref}}}\right)$ is the term considering the effect of the SEI-thickness on reaction. $c_{\text{SEI, ref}}$ is the reference concentration of the SEI. It should be noted that there is no SEI layer protection on the surface of LTO, since its lithiation potential limits reduction of electrolyte components[26]. Thus the value of this term is 1 for LTO anode; W_a is specific intercalated lithium content in jelly roll; H_a is anode-reaction heat release per unit mass. **Table 1** lists the parameter values for graphite and LTO.

Table 1

Thermophysical properties of anode materials[27, 28]

Parameter	lithiated graphite	lithiated Li$_4$Ti$_5$O$_{12}$
A_a	2.5×10^{13}	5.21×10^{19}
Ea_a	1.35×10^5	1.88×10^5
H_a	1.714×10^6	2.568×10^5

2.2.3 Separator melting and internal short circuit

The separator is used to separate the cathode and anode materials to prevent internal short circuit (ISC)[29]. When the temperature reaches the separator's melting point, the separator will shrink, and absorb some heat. After the separator shrinks, the cathode and anode contact together and ISC will occur [9, 30].

The heat released by ISC can be characterized as Eq.(9) and Eq.(10) [31, 32]:

$$\frac{dSoC}{dt} = -T_{ISC}A_{ec}SoC\exp\left(-\frac{Ea_{ec}}{RT}\right) \tag{9}$$

$$Q_{ec} = -\frac{3600\eta \cdot V \cdot C}{V_{cell}} \cdot \frac{dSoC}{dt} \tag{10}$$

where SoC ranges from 0 to 1; T_{ISC} is an extra factor to ensure that ISC occurs only after the separator

melts. When the temperature is higher than separator's melting point, T_{ISC} value is 1, otherwise is 0. In Eq.(10),

η is an efficiency factor; C is the capacity of the cell; V is the voltage of the cell; V_{cell} is the volume of cell.

2.2.4 Reaction between cathode and electrolyte

The cathode will decompose exothermically and release oxygen at onset temperature. The reaction can

be expressed in Eq.(11)[17]:

$$\frac{d\alpha_c}{dt} = A_c\alpha_c(1-\alpha_c)\exp\left(-\frac{Ea_c}{RT}\right) \tag{11}$$

The corresponding heat release per unit volume can be determined as follows:

$$Q_c = W_cH_c\frac{d\alpha_c}{dt} \tag{12}$$

where α_c is the degree of conversion; A_c is the frequency factor; Ea_c is the activation energy; W_c is

specific cathode content in jelly roll; H_c is cathode-reaction heat release per unit mass. **Table 2** summarize

the parameter values specified for various cathode materials in the simulations.

Table 2

Thermophysical properties of cathode materials[18, 19, 23, 33]

Parameter	$LiCoO_2$	$LiNi_{0.8}Co_{0.15}Al_{0.05}O_2$	$Li_{1.1}(Ni_{1/3}Co_{1/3}Mn_{1/3})_{0.9}O_2$	$LiFePO_4$
A_c	3.14×10^5	2.18×10^5	7.9×10^5	1.947×10^5
Ea_c	6.667×10^{13}	7.25×10^{16}	2.25×10^{14}	2.0×10^8
H_c	1.396×10^5	1.3×10^5	1.54×10^5	1.03×10^5
W_c	1.3×10^3	1.274×10^3	1.293×10^3	0.96×10^3

2.2.5 Decomposition of electrolyte

In addition to react with anode and cathode, electrolyte will decompose exothermically during TR. The

reaction can be expressed in Eq.(13)[18]:

$$\frac{dc_e}{dt} = -A_e c_e \exp\left(-\frac{Ea_e}{RT}\right) \tag{13}$$

And the heat release per unit volume due to the decomposition of electrolyte is determined as follows:

$$Q_e = -W_e H_e \frac{dc_e}{dt} \tag{14}$$

where c_e is dimensionless amount of electrolyte; A_e is the frequency factor; Ea_e is the activation energy; W_e is specific electrolyte content in jelly roll; H_e is decomposition heat release of electrolyte per unit mass.

Table 3 summarize the parameter values specified for various electrolyte in the simulations.

Table 3

Thermophysical properties of electrolyte materials[34]

Parameter	LiPF$_6$/ EC : DEC	LiPF$_6$/ EC : DMC	LiPF$_6$/ PC : DEC	LiPF$_6$/ PC : DEC
A_e	1.49×10^{115}	1.95×10^{40}	3.92×10^{71}	7.53×10^{19}
Ea$_e$	1.015×10^6	3.742×10^5	6.333×10^5	1.882×10^5
H_e	1.635×10^5	2.312×10^5	3.128×10^5	3.209×10^5

2.2.6 Binder reaction

The binder is used for providing maintaining integrity of the electrodes and sufficient mechanical strength. But when the cell temperature is above 533 K, the binder can react with the cathode material and Li$_x$C$_6$ and release heat[10, 11]. The reaction can be expressed in Eq.(15)[24]:

$$\frac{dc_{PVDF}}{dt} = -A_{PVDF} c_{PVDF} \exp\left(-\frac{Ea_{PVDF}}{RT}\right) \tag{15}$$

The heat release per unit volume is calculated as follows:

$$Q_{PVDF} = -W_{PVDF} H_{PVDF} \frac{dc_{PVDF}}{dt} \tag{16}$$

where c_{PVDF} is dimensionless amount of binder; A_{PVDF} is the frequency factor; Ea_{PVDF} is the activation energy; W_{PVDF} is specific binder content in jelly roll; H_{PVDF} is decomposition heat release of binder per unit mass. The values of above-mentioned parameters are listed in **Table 4**.

Table 4

Kinetic and thermodynamic parameters used in the model

Parameters	Value	Unit	Source
A_{SEI}	1.667×10^{15}	s^{-1}	Ref.[17]
A_{ec}	1.4×10^{12}	s^{-1}	Fit
A_{PVDF}	1.917×10^{25}	s^{-1}	Ref.[24]

$c_{SEI,0}$	0.15	-	Ref.[17]
$c_{SEI,ref}$	1	-	Ref.[25]
$c_{a,0}$	0.75	-	Ref.[17]
$c_{e,0}$	1	-	Ref.[18]
$c_{PVDF,0}$	1	-	Ref.[24]
C	3.4	Ah	-
Ea_{SEI}	1.3508×10^5	J mol^{-1}	Ref.[17]
Ea_{ec}	1.17×10^5	J mol^{-1}	Fit
Ea_{PVDF}	2.86×10^5	J mol^{-1}	Ref.[24]
H_{SEI}	2.57×10^5	J kg^{-1}	Ref.[17]
H_{PVDF}	1.5×10^6	J kg^{-1}	Ref.[24]
T_{amb}	300	K	-
V	4.2	V	-
V_{cell}	1.66×10^{-5}	m^3	-
W_{SEI}	194.7	kg m^{-3}	Ref.[17]
W_{PVDF}	81.4	kg m^{-3}	Ref.[24]
$\alpha_{c,0}$	0.04	-	Ref.[17]
η	0.22	-	Ref.[31]
κ	5	W m^{-1} K^{-1}	Fit
ρ	2850	kg m^{-3}	Fit

2.3 Model validation

To validate the developed TR model, some experiments have been carried out to measure the temperature data of the cell under local heating. The battery used for the test was cylindrical 18650 LIB that has a capacity of 3.4 Ah, charge voltage of 4.2 V, nominal voltage of 3.6 V, a diameter of 18 mm and height of 65 mm. The cathode material is $LiNi_{0.8}Co_{0.15}Al_{0.05}O_2$. The anode material is graphite. The electrolyte is $LiPF_6$. The polyimide electrothermal film was used for heating, whose size and power are 30 mm × 62.5 mm and 32.5 W. As shown in **Fig. 3**, the cell and heater were fixed in a specially designed metal holder, exposed to the open air. The K-type thermocouple was attached on the surface of the cell away from the heater to measure the temperature of the LIB cell surface. In the meanwhile, the computer recorded the temperature data measured by the thermocouple, and the camera recorded the progress of experiment. Before heating, the cells charged to 20% SOC and 50% SOC respectively, considering the effect of different SOC. After the TR

was triggered, the power of the heater was cut off immediately.

(a) The experimental devices   (b) Polyimide electrothermal film   (c) 18650 NCA battery
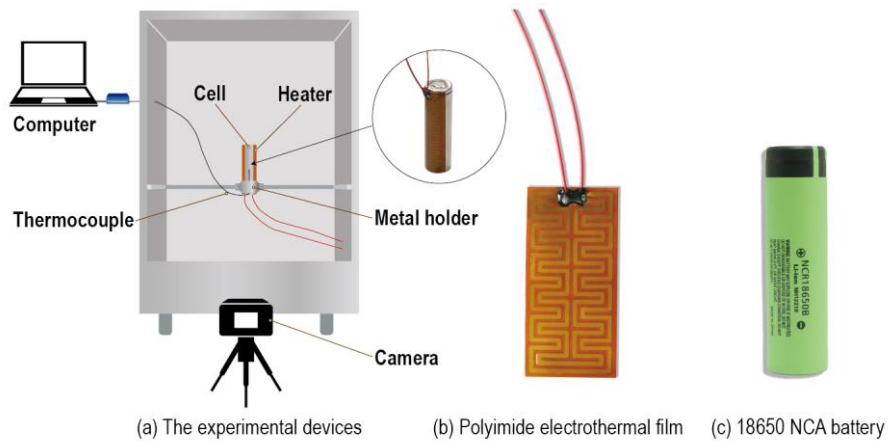
Fig. 3. Schematic of the experimental devices.

Fig. 4 shows the TR behavior of the cell with 20% SOC. After heating for approximately 354 s, the cell

burned violently and released heavy smoke in the meanwhile, showing the TR was triggered. After that, the

flame began to weaken, and completely extinguished at 370 s. However, the cell was still in red-hot state,

indicating that the cell was in high temperature.

0s, start of experiment   354s, thermal runaway   356s   358s   370s

Fig. 4. The TR behavior with 20% SOC.

The prediction of the TR behavior of a cell with different SOC are compared with the experimental

measurements. **Fig. 5** shows the temperature evolution of the cell with 20% and 50% SOC. It can be seen

from **Fig. 6**(a) and (b) that the predicted peak temperature and onset time of TR are close to the measurements.

It should be noted that the simulated temperature is slightly lower than the experimental results both in the

heating stage and the cooling stage after the TR. The marginal deviation is thought to be due to that the

aluminum can containing the jelly roll is not taken into consideration in the simulation, which causes the thermal conductivity of the cell surface layer in the simulation lower than that in the experiment. In this case, the temperature gradient between the heater and the measuring point along the surface layer is larger in the simulation, which leads a lower simulated temperature in the stage of heating. In the stage of cooling, the insulating tape used to fix the thermocouple also affects the heat dissipation of the cell in the experiment, which accounts for the temperature dropping more slowly.
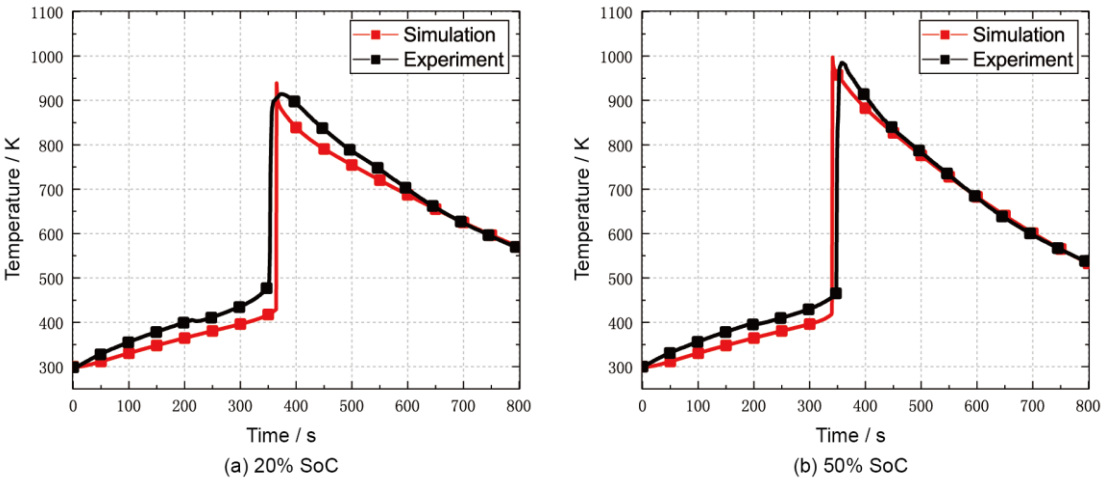

Fig. 5. Comparison of experimental and simulation results.

3. Results and discussion

The TR behaviors of the cells with various materials (i.e. anode, cathode, separator, electrolyte) are simulated to investigate the thermal stability and thermal safety for these materials. The thermal stability reflects the difficulty degree of the TR occurrence when LIBs are under abuse, which can be characterized by the onset time and temperature of TR. The thermal safety reflects the possible hazard of LIBs after TR, which can be characterized by the peak temperature of TR. In addition, to study the effects of external heat and heat loss on the performance of the cell, the influence of various local heating conditions, i.e., heating position, heating area and heating power and various heat dissipation conditions, i.e., ambient temperature

and heat dissipation coefficient on the TR behavior of LIB cell are also numerically investigated.

3.1 The effect of various battery materials

3.1.1 Different anode materials

As graphite and $Li_4Ti_5O_{12}$ (LTO) are widely used materials for the anode of LIBs, the thermal behavior of LTO/NCA cell and the graphite/NCA cell was first numerically investigated under the same heating conditions. The plot in **Fig. 6** compares the temperature curves of the cells with LTO and graphite anode under the heating power of 500 W m^{-2} and 1000 W m^{-2}. It can be found from **Fig. 6**(a) that the when the heating power is 500 W m^{-2}, the onset temperature of TR for LTO cell is 437 K, which is higher than that for graphite cell (407 K). It can also be found from **Fig. 6**(a) that the onset time of TR for the cell with graphite anode is 650 s earlier than that of the cells with LTO anode. When the heating power increases to 1000 W m^{-2}, the onset time difference still exists but is shortened to 150 s, as shown in **Fig. 6**(b). In addition, the peak temperature of TR for LTO cell is 705 K, which is much lower than that of 917 K for the cell with graphite anode. The above differences are believed to be due to the SEI protection. In contrast to graphite, LTO cell is generally considered to possess no SEI protection. Consequently, the exothermic process due to the decomposition of SEI layer to accumulated heat lacks for LTO cells[26], which leads that the temperature rise of the LTO cell is slower than the graphite cell at the point of SEI layer decomposition. As a result, the onset time of TR is longer for the LTO cell. As for the difference of peak temperature of TR, it is because the reaction between graphite anode and electrolyte releases more enthalpy due to the higher energy density of lithiated graphite compared to the lithiated LTO anode[35]. In summary, the simulation results indicate the LIBs with LTO anode show better thermal stability and thermal safety than that with the graphite anode.
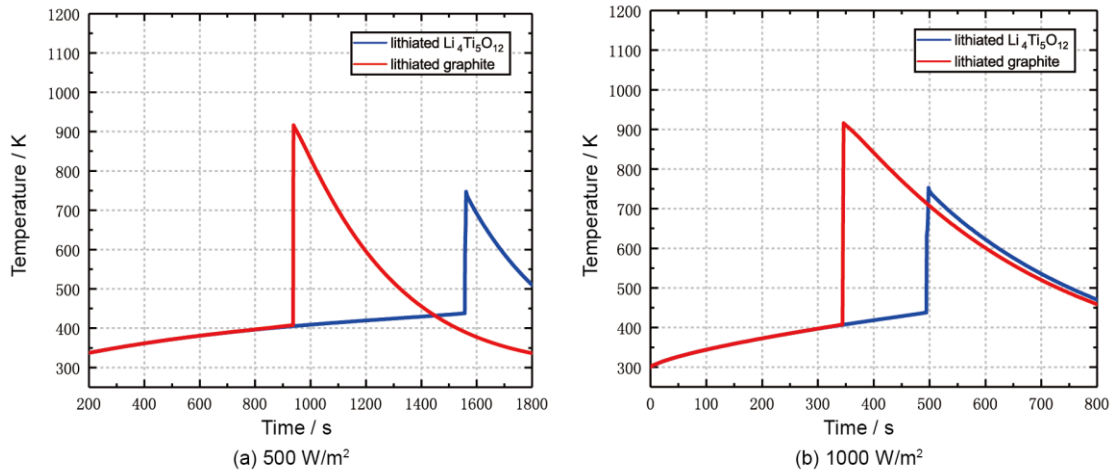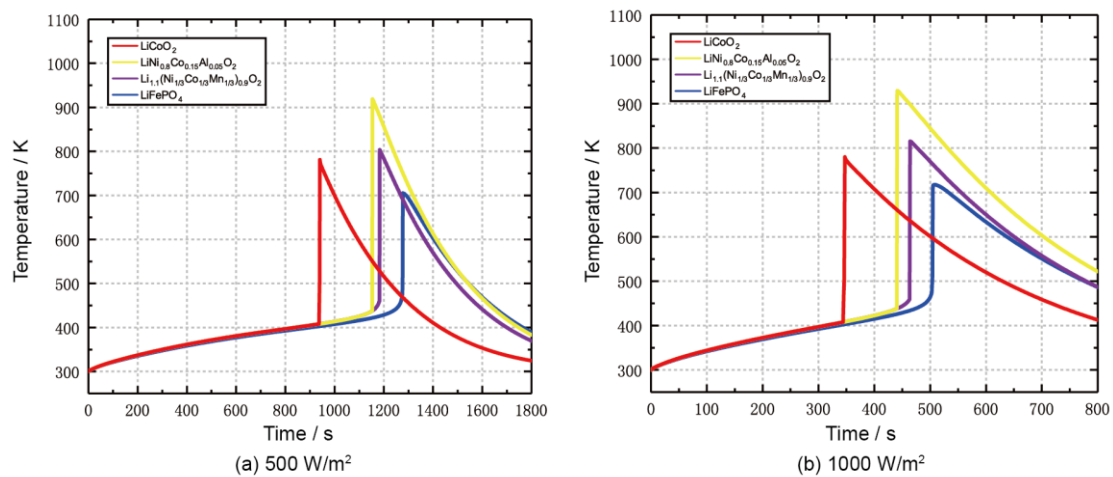
Fig. 6. The temperature variations of cells with graphite and LTO anode under the heating power of 500 and 1000 W m^{-2}.

3.1.2 Different cathode materials

The reaction of cathode and electrolyte contributes the main heat generation to TR[23], thus the investigation of the thermal performance of cathode materials is of great significance to evaluate the hazard of possible TR. This section compares the TR behavior of the batteries with four common used cathode materials, including LiFePO$_4$ (LFP), Li$_{1.1}$(Ni$_{1/3}$Co$_{1/3}$Mn$_{1/3}$)$_{0.9}$O$_2$ (NCM), LiNi$_{0.8}$Co$_{0.15}$Al$_{0.05}$O$_2$ (NCA) and LiCoO$_2$ (LCO). **Fig. 7** shows the evolution of the temperature rise of the cell with various cathode materials under the heating power of 500 W m^{-2} and 1000 W m^{-2}. **Fig. 7**(a) shows the TR onset temperatures are 407 K, 437 K, 457 K and 475 K for LCO cell, NCA cell, NCM cell and LFP cell respectively. Correspondingly, the onset time of TR increase with the increasing TR onset temperature, which is 940 s, 1153 s, 1185 s and 1276 s for LCO cell, NCA cell, NCM cell and LFP cell when the heating power is 500 W m^{-2}. When the heating power increases to 1000 W m^{-2}, it can be found that the TR onset temperature keeps constant but the onset time of TR is shorten to 345 s, 440 s, 462 s and 503 s for LCO cell, NCA cell, NCM cell and LFP cell respectively, as shown in **Fig. 7**(b). Thus, the thermal stability order of the LIBs with different cathode materials can be ranked as: LFP cell > NCA cell > NCM cell > LCO cell. The different peak temperature of TR results from the difference of heat generation of cathode materials, which also reflects the thermal safety

of LIBs. Seen from **Fig. 7**(a) and **Fig. 7**(b), the peak temperatures are about 780 K, 929 K, 815 K and 717 K

for LCO cell, NCA cell, NCM cell and LFP cell respectively. The simulation results indicate that the

decomposition of NCA cathode releases the most enthalpy compared to others, which means it may cause

more serious hazard than other LIBs. Hence the thermal safety order of the LIBs with different cathode is:

LFP cell > LCO cell > NCA cell > NCM cell. It can be found that the diversification of cathode materials has

a significant impact on the TR behaviors of the LIBs, mainly reflected in the onset temperature and onset

time as well as the peak temperature of TR. In addition, the thermal safety and thermal stability of above

cathode materials are consistent with previous results measured under oven tests[23], which means the

change of thermal abuse measures does not impact the thermal safety and thermal stability ranks of LIBs,
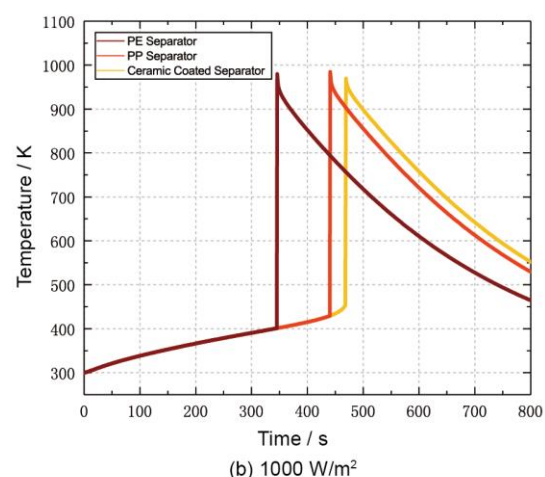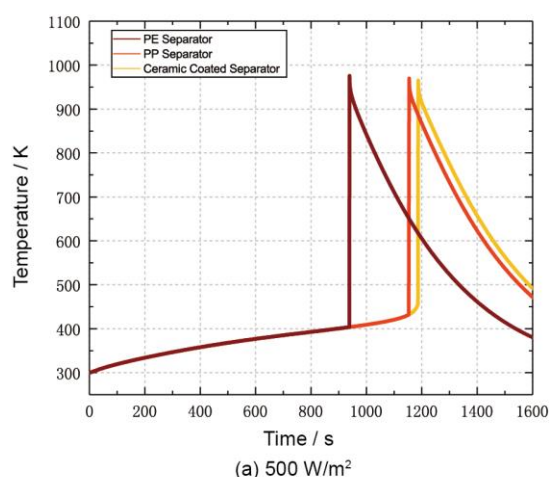
regardless of oven tests or local heating.

Fig. 7. The temperature variations of cells with different cathode material under the heating power of 500 and 1000 W m^{-2}.
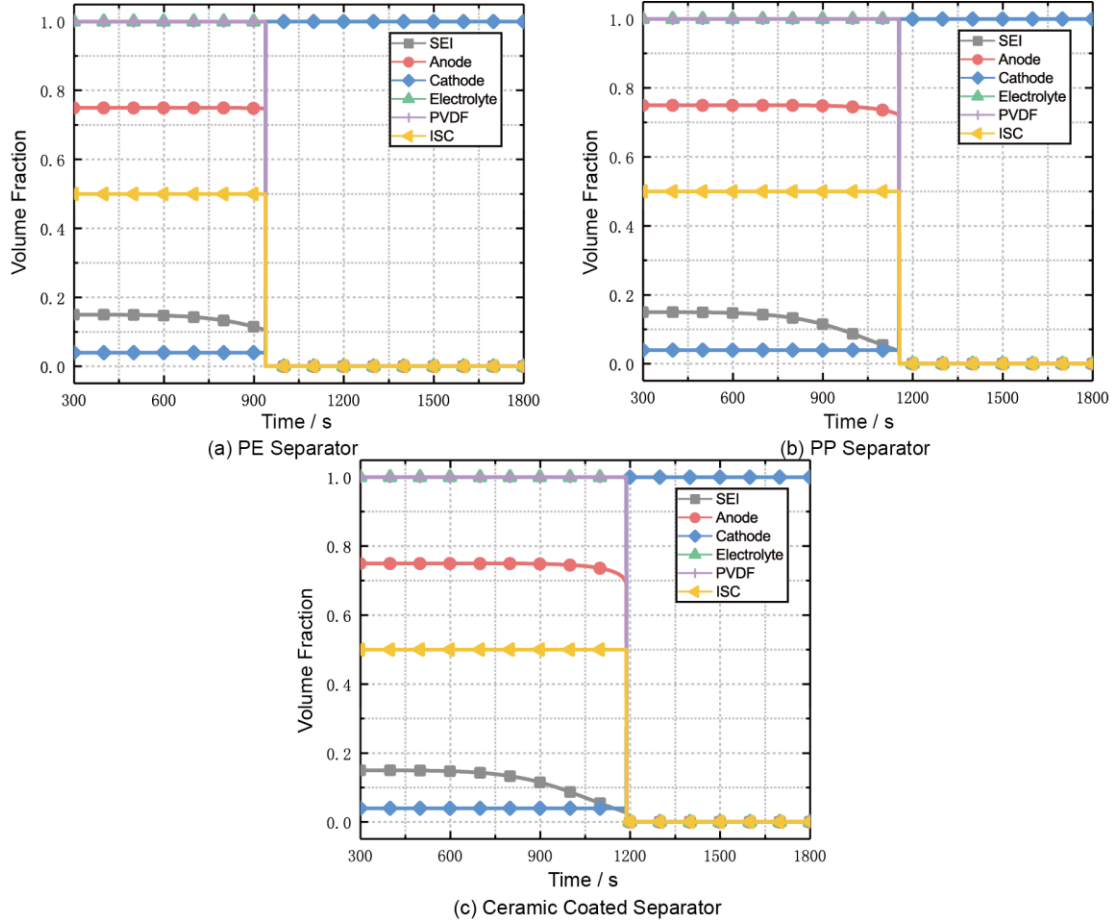
3.1.3 Different separator materials

Almost all the TR accidents are accompanied with ISC[9]. When the ISC occurs, the electric energy

stored in the cell converts spontaneously to heat, which accelerates the chemical reactions and rapidly

increases internal temperature inside the cell. The occurrence of ISC is related to the melting point of the

separator. In order to investigate the influence of different separator materials on the TR of LIB cells, three

common-used separator materials, polyethylene (PE), polypropylene (PP) and ceramic coated separator are considered in this study. The melting point for PE, PP and ceramic coated separator are approximately 408 K, 439 K, and 473 K, respectively[5, 36]. **Fig. 8** shows the variation of temperature rises of the cell with different separator materials. From **Fig. 8**(a) it can be seen that the rate of temperature rise keeps consistent at the stage of heating before TR. As the heating continues, TR occurs for the cell with separator of PE at the onset temperature of 403 K firstly, 431 K for the cell with PP separator and 456 K for the cell with ceramic coated separator. And the onset time of TR is 973 s, 1153 s and 1184 s for PE, PP and ceramic coated separator. When the heating power increases to 1000 W m^{-2}, it can be found that the change trend of temperature is similar but the onset time of TR becomes 344 s, 439 s and 467 s because the increasing heating power shortens the onset time of TR. The results indicate that the onset temperature increases with the increasing melting point of separator, but slightly lower than the melting point. Correspondingly, the onset time of TR also increases with the increasing melting point of separator. In addition, it is noteworthy that the peak temperature keeps the same for the cell with various separators, which indicates the different melting points of separator materials have little impact on the release of electrical and chemical energy stored inside the cell once TR occurs. Totally, the increase of the separator melting point is beneficial to improve the thermal stability of LIBs, while it does not impact the thermal safety.

(a) 500 W/m^2 (b) 1000 W/m^2

Fig. 8. The temperature variations of cells with different separator materials under the heating power of 500 and 1000 W m^{-2}.

It can also be found from **Fig. 8**(a) that as the melting point of cell separator increases from 408 K to 438 K (from PE to PP), the time of initiating TR reduces by 215 s. However, as the melting point increases from 438 K to 473 K, the onset time is only reduced by 53 s, and the trend is similar in **Fig. 8**(b). It turns out that the cell separator with high melting point can relieve the occurrence of TR to some extent. However, when the melting point of separator is up to a certain value, the effects of relief may be no longer remarkable.

Fig. 9 shows the volume fraction of chemical components variation of the cells with different separator materials, with the heating power of 500 W m^{-2}, which may reveal the reasons for the above phenomenon. It can be seen that the SEI layer starts to decompose at 600 s at first, and the anode then starts to decompose with a quite low rate at 766 s. As time goes on, the volume fraction of remaining chemical components drops to zero suddenly, and the TR occurs. As shown in **Fig. 9**(a), the volume fraction of SEI layer and anode reduces about 4.64% and 0.76% before TR for PE separator, which indicates the heat triggering TR mainly comes from external heating. However, the volume fraction of SEI layer and anode reduces about 12.33% and 30.07% before TR for the ceramic coated separator as shown in **Fig. 9**(b), which indicates the decomposition of SEI layer and anode also provides part of the heat for triggering TR. Hence, as the melting point of separator increases to a specific value, the heat that triggers TR not only comes from the external heating power, but also heat generation of side-reactions. In this case, the improvement in thermal stability of LIBs may be less significant. Besides, even if the melting point of cell separator raises to an extremely high temperature, TR also takes place due to the decomposition reaction of electrolyte and binder.

Fig. 9. The volume fraction of chemical component variations of the cells with different separator materials.

3.1.4 Different electrolyte materials

Traditional electrolyte is usually a nonaqueous system composed of organic carbonate solvent and LiPF$_6$.

Common used electrolyte organic solvents include ethylene carbonate (EC), propylene carbonate (PC),

dimethyl carbonate (DMC), diethyl carbonate (DEC)[37]. However, due to the flammability of the organic

solvents and the reactions of electrolyte and lithium embedded into the anode, it usually brings hidden

dangers for the safe use of LIBs. To explore the thermal stability and thermal safety for different electrolytes,

four electrolytes were simulated individually, i.e. 1 M LiPF6 in PC: DEC (1:1 w/w), PC: DMC (1:1 w/w),

EC: DEC (1:1 w/w) and EC: DMC (1:1 w/w), respectively. The cell temperature curves for various electrolyte

materials is presented in **Fig. 10**. It can also be found from **Fig. 10**(a) that the temperature of LIBs with four

electrolytes rises slowly first and TR occurs at about 839 s for the cell of LiPF$_6$ / PC: DMC, 864 s for the cell

of $LiPF_6$ / EC: DMC, 907 s for the cell of $LiPF_6$ / PC: DEC and 939 s for the cell of $LiPF_6$ / EC: DEC. And

the peak temperatures are about 972 K, 948 K, 941 K, 914 K for $LiPF_6$ / EC: DEC, $LiPF_6$ / PC: DEC, $LiPF_6$

/ EC: DMC and $LiPF_6$ / PC: DMC respectively. When the heating power increases to 1000 W m^{-2}, it can be

found from **Fig. 10**(b) that the peak temperature basically unchanged but the onset time of TR decreases to

308 s for the cell of $LiPF_6$ / PC: DMC, 318 s for the cell of $LiPF_6$ / EC: DMC, 333 s for the cell of $LiPF_6$ /

PC: DEC and 345 s for the cell of $LiPF_6$ / EC: DEC. The simulation results show that the difference among

the cells with various electrolytes is mainly reflected in the peak temperature and the trigger time of TR. The

different TR peak temperature of LIBs indicates the difference in thermal safety for electrolyte materials; the

thermal safety order of the electrolyte is: $LiPF_6$ / EC: DEC > $LiPF_6$ / PC: DEC > $LiPF_6$ / EC: DMC > $LiPF_6$ /

PC: DMC. And the thermal stability order of the electrolyte is: $LiPF_6$ / EC: DEC > $LiPF_6$ / PC: DEC > $LiPF_6$

/ EC: DMC > $LiPF_6$ / PC: DMC. However, compared to the study of previous sections, it can be found that

the change of electrolyte has little significant effect on the peak temperature and onset time of TR, which

means it does not play a dominant role in determining thermal behaviors of cells under local heating.
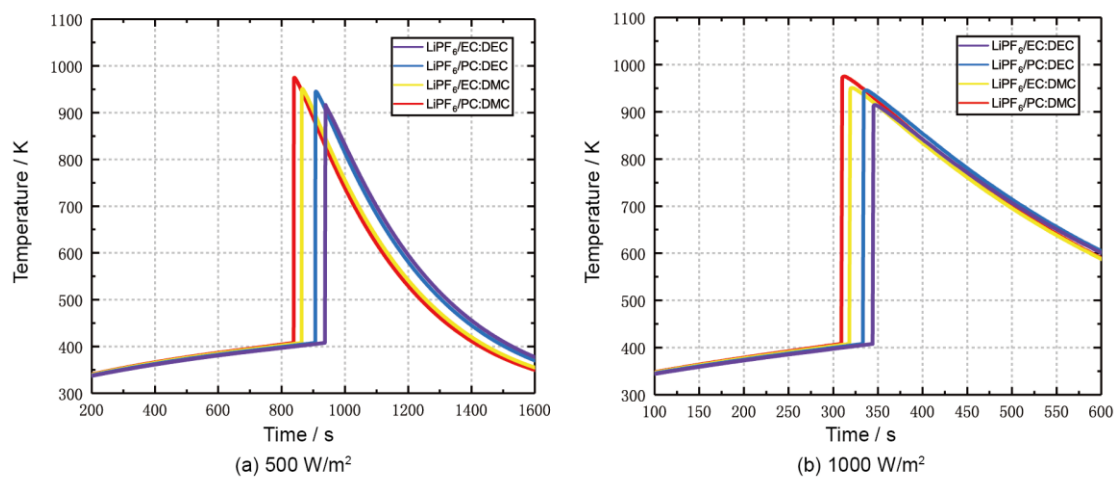
Fig. 10. The temperature variations of cells with different electrolyte under the heating power of 500 and 1000 W m^{-2}.

3.2 The effect of external heating conditions

3.2.1 Different heating position

Owing to the various connection modes among the cells in the LIB pack, the cell may receive heat at different positions during TR propagation. To investigate the effect of different heating positions on the thermal behavior of the cell and identify weak spots inducing TR, three local heating positions are considered in this study for the graphite/NCA cell: a circular heater of 9 mm is located on the middle, end and bottom of the cell.

Fig. 11 displays the thermal failure propagation in the cell heated by different positions. The TR process of the cell can be summarized in three stages: (1) heating stage: the local temperature of the cell starts to rise but the rate of temperature rise is quite slow. Besides, the simulation results indicate the temperature difference on the cell surface is smaller while the average temperature shows a larger value when heating on the middle of the cell compared with other positions. The heating stage ends at about 271 s for the heating position of middle, 139 s for the heating position of end and 106 s for the heating position of the bottom. (2) TR stage: a region with extremely high temperature appears near the heating position and spreads to the region where TR has not occurred until the entire cell is involved in TR. Due to the huge temperature gradient inside the battery, this process can be typically completed within a few seconds. The duration of TR stage is different for different heating positions, which is about 1.5 s for the heating position of middle, 4.5 s for the heating position of end and 5 s for the heating position of the bottom. (3) cooling stage: the cell is cooled to surrounding temperature ascribed to the end of exothermic decomposition reactions.
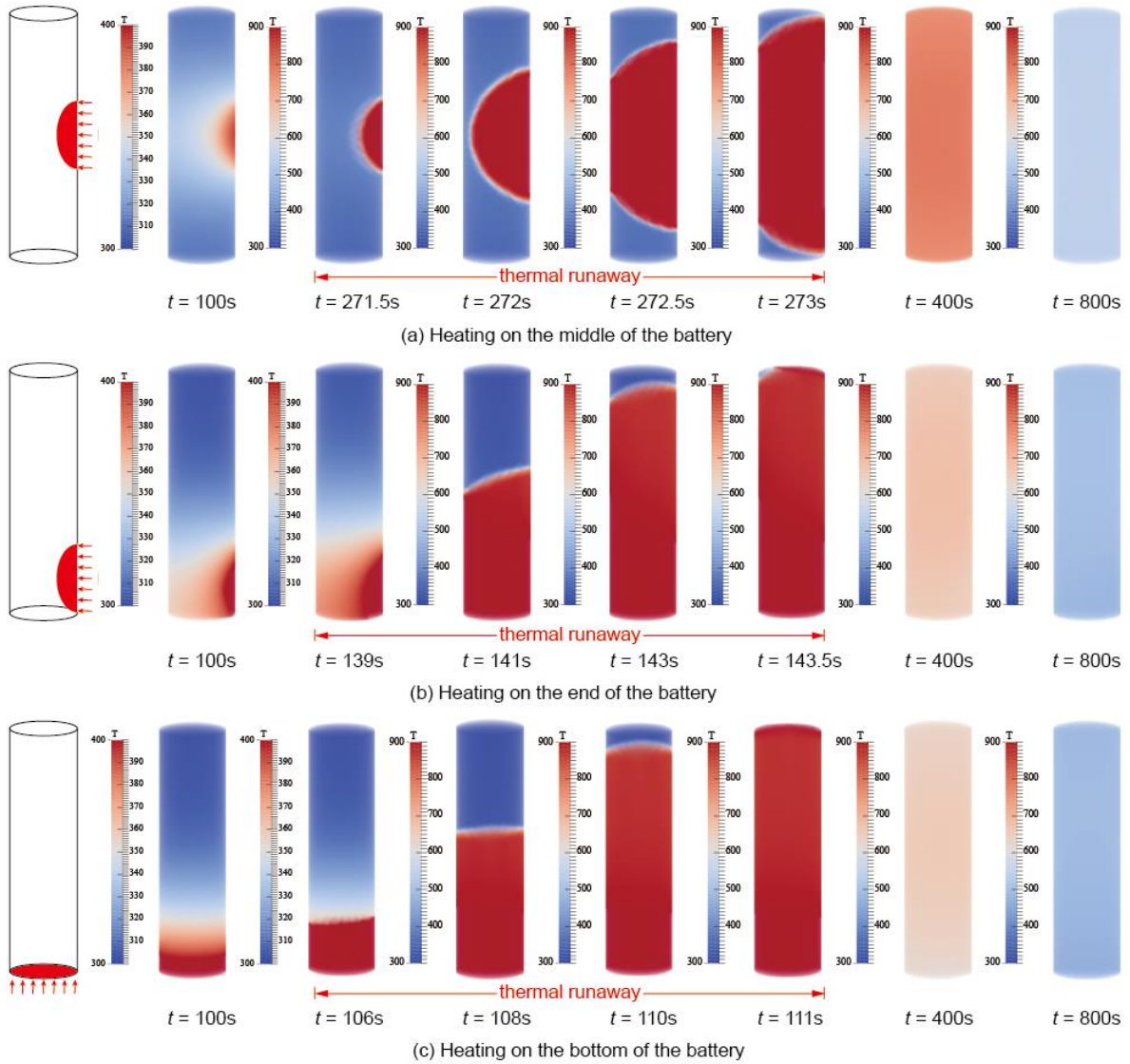
Fig. 11. The simulation results of the temperature evolution at different positions with heating power of 6000 W m⁻².

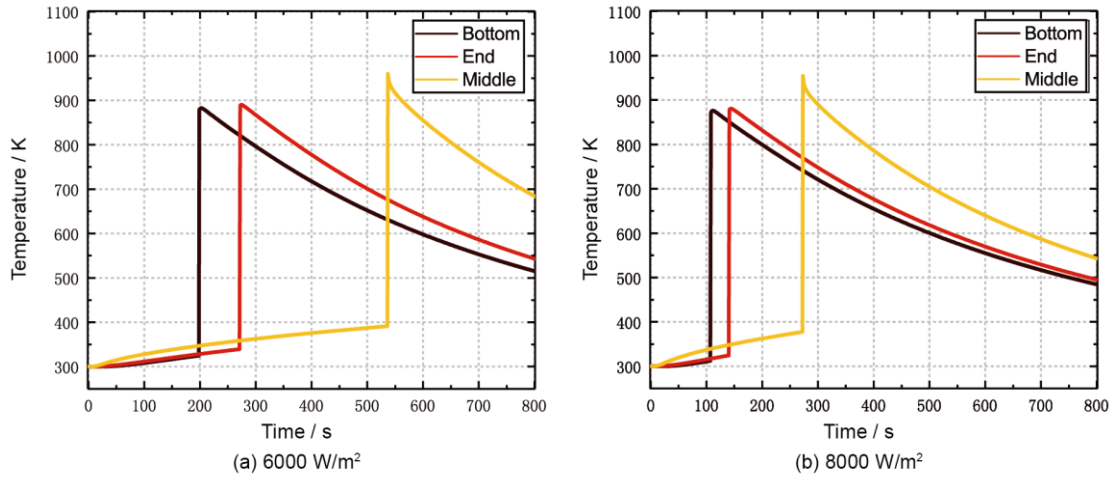The temperature rises curves at different heating positions are shown at **Fig. 12**. With the heating power of 6000 W m⁻², the onset time of TR is 200 s, 272 s, 536 s at the position of bottom, end and middle respectively, and the time is 108 s, 141 s and 273 s for the heating power of 8000 W m⁻². It can be found that the heating position near the bottom of cell triggers the TR of LIB earlier than the other two positions, indicating that this heating position leads to a high probability of thermal failure. In heating stage, the temperature rise of cell is determined by the heat flowing into the cell from external heating that is identical for various heating positions owing to the same heating condition and the heat flowing out from the cell that makes major contributions, from the perspective of lumped model. The heat flowing out from the cell Q_{out} is

calculated as follows:

$$Q_{out} = hS(T_{amb} - T_{sur}) + \varepsilon\sigma S(T_{amb}^4 - T_{sur}^4) \tag{17}$$

where S is the heat dissipation area, T_{sur} is the average temperature of the cell surface. As mentioned above, heating on the bottom of the cell shows lower average surface temperature than heating on the end and middle, which makes the heat loss lower than other heating positions in heating stage. In this case, the temperature rise rate is largest, causing TR to occur sooner than other heating positions. In addition, owing to the longer transfer path, the heat is easier to accumulate making the cell core temperature higher when heating on the bottom of the cell. Thereby when the local heating position is near the bottom of the cell, the probability of TR is higher than other heating positions. Therefore, some insulation measures should be taken on the ends of the cell to reduce the risk of thermal abuse in the battery BMS.
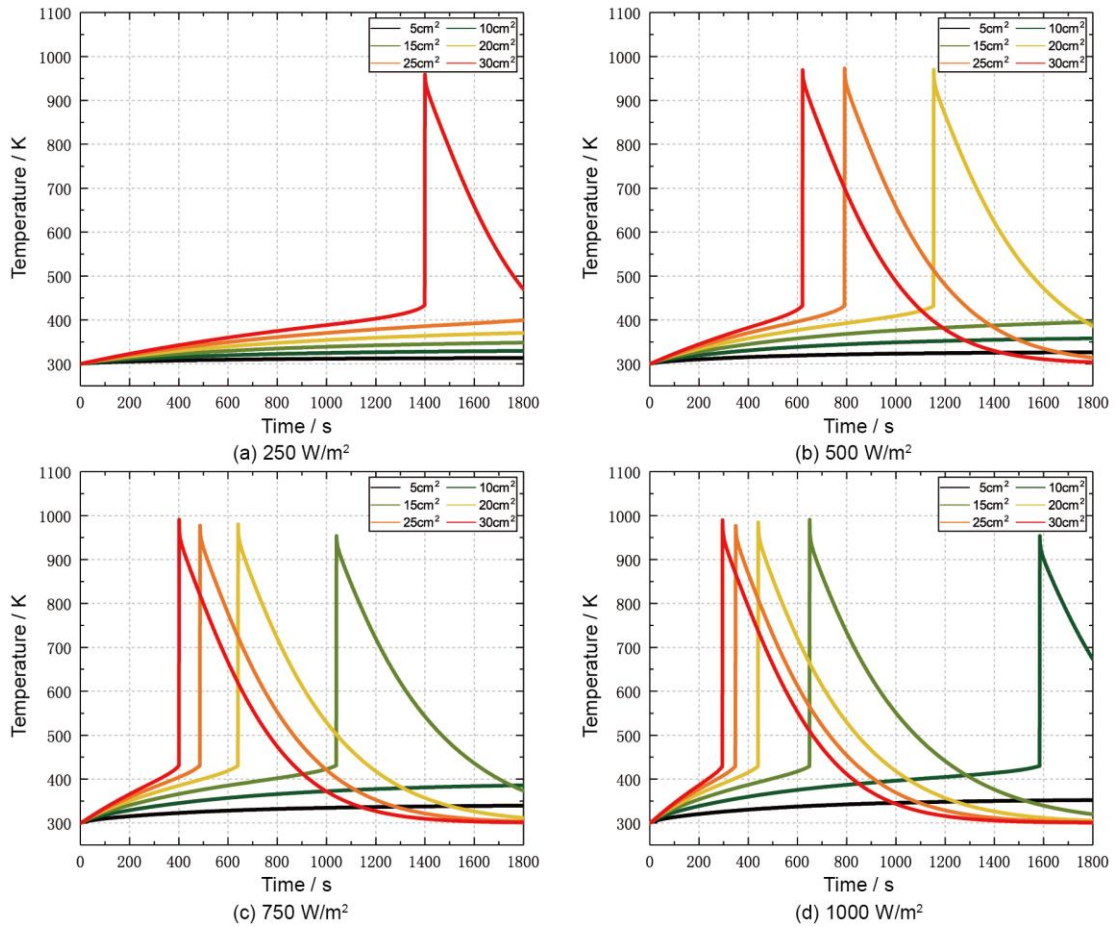

Fig. 12. The temperature variations of cells under local heating at different positions with the heating power of 6000 and 8000 W m^{-2}

3.2.2 Different heating area and heating power

The constant-power single-cell heating test is often used to determine under what conditions the cell is most susceptible to TR. To ascertain the probability and severity of TR under various heating conditions, a series of simulations have been conducted, at the ambient temperature of 300 K and the convection coefficient of 15 W m^{-2} K^{-1}, which is a typical heat dissipation condition without forced convection heat transfer. **Fig.**

13 shows the cell temperature variation under different heating power ranging from 250 to 1000 W m^{-2} and the heating size from 5 to 30 cm^2. As shown in **Fig. 13**(a), for the heating power of 250 W m^{-2}, the cells heated with the heating area of 5 cm^2, 10 cm^2 and 15 cm^2 stay in steady-state condition after heating 1800 s. But for cells heated with the heating area of 20 cm^2 and 30 cm^2, the trend of temperature rise still exists at 1800 s, and the cell heated by the heater with the area of 30 cm^2 goes into TR at about 1400 s. When the heating power increases to 500 W m^{-2}, it can be seen that the initial temperature rise and the number of cells into TR increase. The cells heated by the heater with the area of 20 cm^2 and 25 cm^2 also go into TR and their onset time of TR is 792 s and 1155 s, as shown in **Fig. 13**(b). And the onset time of TR decreases to 610 s for the cell with heating area of 30 cm^2. As the heating power increases to 750 W m^{-2}, the cell heated with heating area of 15 cm^2 also goes into TR at 1038 s. And TR does not occur for the cell with heating area of 5 cm^2 when the heating power rises to 1000 W m^{-2} , as shown in **Fig. 13**(d). It can be seen that the higher heating power and larger heating area speed up the initial temperature rise and trigger TR earlier than lower value. In addition, it is noted that the total power (heating area S × heating power q) applied to the cells of TR is larger than 1.0 W, and the minimum of total power that does not trigger TR is 0.75 W, which means the critical value of the total power that can trigger TR may be between 0.75W and 1.0W. In other words, when the total power applied to the cell surface is less than 0.75 W, such heating does not lead the cell into TR and the cells stay in steady-state condition. Different from the previous research results under oven test[21, 23], the peak temperature is little influenced by the various heating conditions in this study while the peak temperature increases with the oven temperature under oven test. The reason may lie in that only the side-reactions whose onset temperature is lower than the oven temperature can proceed for the cell under oven test. Hence the side-reactions within the cell may not all proceed at low oven temperature. These simulation results provide insights for the safe design of BMS of battery packs to reduce the probability of thermal

propagation after TR: Some measures such as increasing the contact thermal resistance should be taken to reduce the heat flux between the cells. In addition, the contact areas between the batteries should be reduced.

Fig. 13. The temperature variations of cells with the heating size from 5 to 30 cm^2 and the heating power from 250 to 1000 W m^{-2}.

3.3 The effect of heat dissipation conditions

Air cooling and liquid cooling are widely-used cooling techniques in battery BMS, the essence of which is enhancing convection condition and reducing ambient temperature to remove heat[38]. To study the effects of convection condition and ambient temperature on the TR behaviors, a series of simulations have been implemented. **Fig. 14** shows the cell temperature variation under different ambient temperature ranging from 260 to 320 K and the convection coefficient from 10 to 50 W m^{-2} K^{-1}. **Fig. 14**(a) shows the temperature rises curves at h = 10, 20, 30, 40, 50 W m^{-2} K^{-1} at the ambient temperature of 260 K. It can be found that only the

cell cooled with the convection coefficient of 10 W m^{-2} K^{-1} goes into TR at 975 s. And the cells cooled with the convection coefficient of 30, 40 and 50 W m^{-2} K^{-1} stay in steady-state condition at 380 K, 361 K and 346 K. As the ambient temperature increases to 280 K, the number of cells into TR increases: the cell with the convection coefficient of 20 W m^{-2} K^{-1} also goes into TR. In addition, the steady-state temperature of cells without TR also increases about 20 K comparing the ambient temperature of 260 K. When the ambient temperature increases to 300 K, TR is observed for the cell cooled with the convection coefficient of 10, 20 and 30 W m^{-2} K^{-1} at 650 s, 828 s and 1284 s. And for the cells not going into TR, the steady-state temperature increases about 37 K comparing **Fig. 14**(a). When the ambient temperature increases to 320 K, only the cell cooled with the convection coefficient 50 W m^{-2} K^{-1} can stay in steady-state condition. Comparing the temperature rise curves at the same ambient temperature, the simulation results indicate the increase of heat dissipation coefficient delays the onset time of TR or even prevents the cell from TR to steady-state condition of temperature. Further analysis for the cells not going into TR shows that the high heat dissipation coefficient helps the cell steady-state temperature close to the surrounding temperature. When the heat loss on the cell surface and heat from external source as well as generated from side-reactions are balanced, the cells can stay in steady-state condition, but once the temperature of the cells before reaching steady-state condition is higher than the onset temperature of TR, TR may occur. The increasing heat dissipation coefficient directly increases the heat loss on the cell surface, which decreases the initial temperature rise of the cell and makes it stay in steady-state condition at low temperature. In addition, the heat loss of the cell also depends on the temperature difference between the cell surface and environment during heating stage. The low ambient temperature increases the temperature difference and the heat from external heating as well as generated from side-reactions is more easily dissipated to the environment in this case. Thus, the low ambient temperature can delay the simulated onset time of TR or prevents TR and the steady-state temperature of the cells

decreases with the decreasing ambient temperature.

The above results and analysis reveal the reason why there is more frequent TR accidents in hot weather, and provide inspiration on the inhibition on thermal propagation: for one thing, the heat transfer condition should be improved, such as increasing the velocity of airflow to increase convective heat transfer coefficient of the cell surface. For another, it should make the ambient temperature stay at low point such as adopting phase change material (PCM) as passive cooling method of BMS.
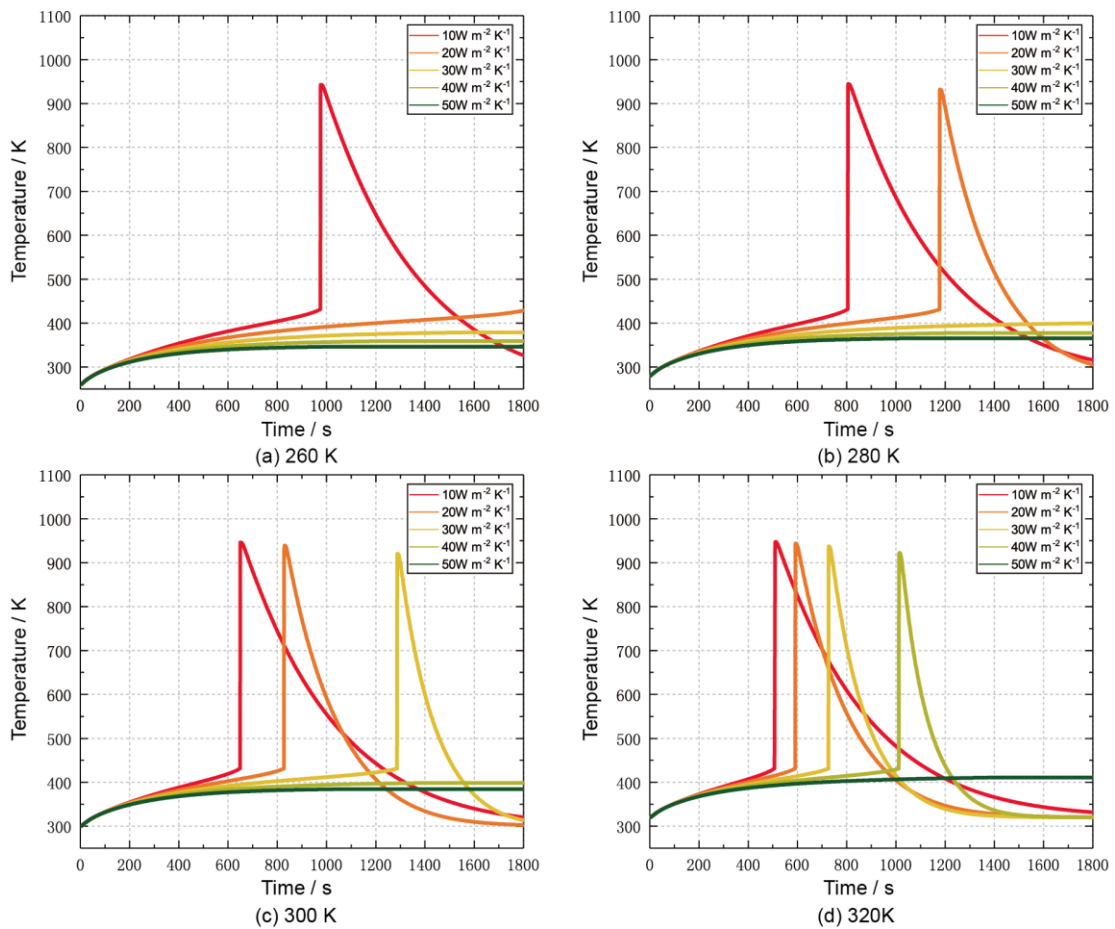
Fig. 14. The temperature variations of cells with the ambient temperature from 260 to 320 K and the convection coefficient from 10 to 50 W m^{-2} K^{-1}.

4. Conclusions

Aiming at systematically studying the TR risk of the cells under local heating conditions as well as numerically investigating the difference in thermal stability and thermal safety for various battery materials,

a three-dimensional model coupling heat transfer and electrochemistry is built in OpenFOAM, where five exothermic chemical reactions and ISC are considered. The model has been validated against experiments of graphite/NCA battery TR triggered by local heating. Subsequent simulations have also been conducted using the validated model, investigating and analyzing the effects of heat generation, external heat and heat loss by simulating TR behaviors with various battery materials (i.e. anode, cathode, separator, electrolyte), external heating conditions (i.e. heating position, heating area, heating power) and heat dissipation conditions (i.e. ambient temperature, heat dissipation coefficient) respectively. Additionally, some simulation results have been visualized to reveal the cell-internal propagation of TR under local heating, and the other specific conclusions are summarized as follows:

(1) The LIBs with LTO anode show more outstanding thermal safety and stability than the LIBs with graphite anode. The thermal safety order of the LIBs with different cathode is: LFP cell > NCM cell > NCA cell > LCO cell, and the thermal stability order of the LIBs with different cathode is: LFP cell > LCO cell > NCM cell > NCA cell. The increasing melting temperature of separator is found to provide effective mitigation against the premature occurrence of TR but less effective when the melting point is higher than a specific value. In addition, the separator doesn't impact the thermal safety of LIBs. Compared to other battery materials, the variety of electrolyte shows limited effects on the thermal safety and thermal stability of LIBs.

(2) When heating near the bottom of the cell, the probability of TR is higher than other heating positions, so the protection near both ends of the cell should be strengthened. The higher heating power and larger heating area speed up the initial temperature rise and trigger TR earlier than lower value. When the total power applied to the cell surface is less than 0.75 W at 300K and the convection coefficient of 15 W m^{-2} K^{-1}, no TR behavior is observed.

(3) The increasing heat dissipation coefficient and reducing ambient temperature delay the onset of TR

or make the cell from TR to steady-state condition of temperature. The steady-state temperature is closer to the ambient temperature as the heat dissipation conditions improve. So an available BMS is the key to preventing TR of lithium-ion batteries.

These above conclusions may provide significant guidance for the safe design of BMS of battery packs. In addition, relying on the open source frame of OpenFOAM, this model can be easily applied to other commercial batteries as well as the newly developed batteries in the future, which provides a great deal of convenience for assisting risk analysis of BMS.

Acknowledgements

References

[1] Zhang J, Zhang L, Sun F, Wang Z. An Overview on Thermal Safety Issues of Lithium-ion Batteries for Electric Vehicle Application. IEEE Access. 2018;6:23848-63.

[2] Zhao R, Liu J, Gu J. Simulation and experimental study on lithium ion battery short circuit. Applied Energy. 2016;173:29-39.

[3] Wang H, Kumar A, Simunovic S, Allu S, Kalnaus S, Turner JA, et al. Progressive mechanical indentation of large-format Li-ion cells. Journal of Power Sources. 2017;341:156-64.

[4] Ma T, Chen L, Liu S, Zhang Z, Xiao S, Fan B, et al. Mechanics-morphologic coupling studies of commercialized lithium-ion batteries under nail penetration test. Journal of Power Sources. 2019;437:226928.

[5] Mao B, Chen H, Cui Z, Wu T, Wang Q. Failure mechanism of the lithium ion battery during nail penetration. International Journal of Heat and Mass Transfer. 2018;122:1103-15.

[6] Ren D, Feng X, Lu L, He X, Ouyang M. Overcharge behaviors and failure mechanism of lithium-ion batteries under different test conditions. Applied Energy. 2019;250:323-32.

[7] Ye J, Chen H, Wang Q, Huang P, Sun J, Lo S. Thermal behavior and failure mechanism of lithium ion cells during overcharge under adiabatic conditions. Applied Energy. 2016;182:464-74.

[8] Ren D, Liu X, Feng X, Lu L, Ouyang M, Li J, et al. Model-based thermal runaway prediction of lithium-ion batteries from kinetics analysis of cell components. Applied Energy. 2018;228:633-44.

[9] Feng X, Ouyang M, Liu X, Lu L, Xia Y, He X. Thermal runaway mechanism of lithium ion battery for electric

vehicles: A review. Energy Storage Materials. 2018;10:246-67.

[10] Wang Q, Mao B, Stoliarov SI, Sun J. A review of lithium ion battery failure mechanisms and fire prevention strategies. Progress in Energy and Combustion Science. 2019;73:95-131.

[11] Wang Q, Ping P, Zhao X, Chu G, Sun J, Chen C. Thermal runaway caused fire and explosion of lithium ion battery. Journal of Power Sources. 2012;208:210-24.

[12] Balakrishnan PG, Ramesh R, Prem Kumar T. Safety mechanisms in lithium-ion batteries. Journal of Power Sources. 2006;155:401-14.

[13] Beauregard GPJUDoE, Idaho National Laboratory, Idaho Falls, ID, Report. Report of investigation: Hybrids plus plug in hybrid electric vehicle. 2008.

[14] Weng J, Yang X, Ouyang D, Chen M, Zhang G, Wang J. Comparative study on the transversal/lengthwise thermal failure propagation and heating position effect of lithium-ion batteries. Applied Energy. 2019;255:113761.

[15] Li H, Chen H, Zhong G, Wang Y, Wang Q. Experimental study on thermal runaway risk of 18650 lithium ion battery under side-heating condition. Journal of Loss Prevention in the Process Industries. 2019;61:122-9.

[16] Wang Z, Yang H, Li Y, Wang G, Wang J. Thermal runaway and fire behaviors of large-scale lithium ion batteries with different heating methods. Journal of Hazardous Materials. 2019;379:120730.

[17] Hatchard TD, MacNeil DD, Basu A, JR D. Thermal model of cylindrical and prismatic lithium-ion cells. Electrochem SoC. 2001;148(7):A755.

[18] Kim G-H, Pesaran A, Spotnitz R. A three-dimensional thermal abuse model for lithium-ion cells. Journal of Power Sources. 2007;170:476-89.

[19] Guo G, Long B, Cheng B, Zhou S, Xu P, Cao B. Three-dimensional thermal finite element modeling of lithium-ion battery in thermal abuse application. Journal of Power Sources. 2010;195:2393-8.

[20] Peng P, Sun Y, Jiang F. Thermal analyses of LiCoO2 lithium-ion battery during oven tests. Heat and Mass Transfer. 2014;50:1405-16.

[21] Lopez CF, Jeevarajan JA, Mukherjee PP. Characterization of Lithium-Ion Battery Thermal Abuse Behavior Using Experimental and Computational Analysis. Journal of The Electrochemical Society. 2015;162:A2163-A73.

[22] Lei Z, Maotao Z, Xiaoming X, Junkui G. Thermal runaway characteristics on NCM lithium-ion batteries triggered by local heating under different heat dissipation conditions. Applied Thermal Engineering. 2019;159:113847.

[23] Peng P, Jiang F. Thermal safety of lithium-ion batteries with various cathode materials: A numerical study. International Journal of Heat and Mass Transfer. 2016;103:1008-16.

[24] Zhang M, Feng X, Ouyang M, Lu L, Wang F, Fan B, et al. Experiments and Modeling of Nail Penetration Thermal Runaway in a NCM Li-ion Power Battery. Automotive Engineering. 2015;37:743-50 and 56.

[25] Feng X, He X, Ouyang M, Lu L, Wu P, Kulp C, et al. Thermal runaway propagation model for designing a safer battery pack with 25Ah LiNixCoyMnzO2 large format lithium ion battery. Applied Energy. 2015;154:74-91.

[26] Bernhard R, Metzger M, Gasteiger HA. Gas Evolution at Graphite Anodes Depending on Electrolyte Water Content and SEI Quality Studied by On-Line Electrochemical Mass Spectrometry. Journal of The Electrochemical Society. 2015;162:A1984-A9.

[27] Richard MN, Society JRDJJotE. Accelerating rate calorimetry study on the thermal stability of lithium intercalated graphite in electrolyte I. experimental. 1999.

[28] Huang P, Ping P, Li K, Chen H, Wang Q, Wen J, et al. Experimental and modeling analysis of thermal runaway propagation over the large format energy storage battery module with Li4Ti5O12 anode. Applied Energy. 2016;183:659-73.

[29] Zhang H, Zhou M, Lin C-E, Zhu B-K. Progress in Polymeric Separators for Lithium Ion Batteries. RSC Adv. 2015;5.

[30] Li H, Duan Q, Zhao C, Huang Z, Wang Q. Experimental investigation on the thermal runaway and its propagation in the large format battery module with Li(Ni1/3Co1/3Mn1/3)O2 as cathode. Journal of Hazardous Materials. 2019;375:241-54.

[31] Paul T. Coman, Eric C. Darcy, Christian T. Veje, White RE. Modelling Li-Ion Cell Thermal Runaway Triggered by an Internal Short Circuit Device Using an Efficiency Factor and Arrhenius Formulations. Journal of the Electrochemical Society. 2017;164: A587-A593.

[32] Coman PT, Darcy EC, Veje CT, White RE. Numerical analysis of heat propagation in a battery pack using a novel technology for triggering thermal runaway. Applied Energy. 2017;203:189-200.

[33] Venkatachalapathy R, Lee CW, Lu W, Prakash J. Thermal investigations of transitional metal oxide cathodes in Li-ion cells. Electrochemistry Communications. 2000;2:104-7.

[34] Wang Q, Sun J, Yao X, Chen C. Micro calorimeter study on the thermal stability of lithium-ion battery electrolytes. Journal of Loss Prevention in the Process Industries. 2006;19:561-9.

[35] Belharouak I, Sun YK, Lu W, Amine K. On the Safety of the Li[sub 4]Ti[sub 5]O[sub 12]／LiMn[sub 2]O[sub 4] Lithium-Ion Battery System. Journal of The Electrochemical Society. 2007;154:A1083.

[36] Orendorff CJ. The Role of Separators in Lithium-Ion Cell Safety. The Electrochemical Society Interface. 2012;21:61-5.

[37] Wang Q, Jiang L, Yu Y, Sun J. Progress of enhancing the safety of lithium ion battery from the electrolyte aspect. Nano Energy. 2019;55:93-114.

[38] Jaguemont J, Van Mierlo J. A comprehensive review of future thermal management systems for battery-electrified vehicles. Journal of Energy Storage. 2020;31:101551.